How to cite: *Angew. Chem. Int. Ed.* **2025**, *64*, e202423273
doi.org/10.1002/anie.202423273

Heterogeneous Catalysis | Hot Paper

Single-Step Synthesis of Dimethyl Ether from Syngas over Nanoparticle-Derived Bifunctional $Pd/CeO_2/Al_2O_3$ Catalysts

Bing Wang, Zairan Yu, Shuang Chen, Nicola Da Roit, Dieter Schild, Michael Zimmermann, Yuemin Wang, and Silke Behrens**

Abstract: The single-step syngas-to-dimethyl ether (STD) process offers both economic and technical advantages over the current two-step industrial process that utilizes $Cu/ZnO/Al_2O_3$ catalysts. Here, we report a highly active bifunctional $Pd/CeO_2/\gamma\text{-}Al_2O_3$ catalyst, in which Pd colloids dispersed in a nanoscale CeO_2 matrix serve as the key building block for the methanol-active component, efficiently catalysing the STD reaction. For $Pd/CeO_2/\gamma\text{-}Al_2O_3$ with a high Pd-CeO_2 interface concentration, CO conversion and dimethyl ether yield are significantly increased compared to Pd supported on Al_2O_3. Systematic investigations using spectroscopic and microscopic techniques reveal the formation of highly dispersed palladium clusters/particles confined within the nanoparticulate CeO_2 matrix. The superior catalytic performance in both activity and stability observed for the $Pd/CeO_2/\gamma\text{-}Al_2O_3$ in the STD reaction stems from the active cationic palladium interfacial species and the presence of adjacent O vacancies.

Introduction

The single-step syngas-to-dimethyl ether (STD) synthesis on bifunctional catalysts is of great interest for the valorization of CO_2 and syngas from biomass gasification. The economics of dimethyl ether (DME) (traditionally based on fuel use) are attracting increasing interest, in parallel with the development of various pathways for its conversion to hydrocarbons (such as olefins, oxygenates, aromatics, and liquefied petroleum gas) and H_2 production.[1] DME is currently produced from syngas (CO/H_2) in a two-step process using $Cu/ZnO/Al_2O_3$ catalysts for methanol synthesis and solid acids (e.g., $\gamma\text{-}Al_2O_3$ or zeolites) for its dehydration. By taking advantage of the favorable thermodynamics, the single-step STD process leads to higher syngas conversions with economic and technical benefits (e.g., cost savings due to process simplification).[2] The direct conversion of syngas to DME has recently been advanced by BASF and Linde in a joint effort with a technology that is applicable to medium to large scale DME production and can be operated with a flexible syngas feedstock. The overall STD reaction can be described by equation (1) (for possible reaction pathways see also Figure S10):

$$3\ CO\ +\ 3\ H_2 \leftrightarrow CH_3OCH_3 + CO_2 \qquad (1)$$

The STD process requires catalysts that combine high methanol synthesis and dehydration activity, e.g., by physically combining the methanol and dehydration catalysts[3] or by designing specific bifunctional catalysts by impregnation,[4] co-precipitation,[4a,5] or sol-gel processes.[6] $Cu/ZnO/Al_2O_3$ catalysts have been the focus of most studies to date, but despite their high activity and selectivity in DME synthesis, they often suffer from deactivation.[7] Recently, Pd-based catalysts have emerged as an interesting alternative with high selectivity and good thermal stability. For example, Pd/Zn- and Pd/Ga-based nanoparticles (NPs) have been used as precursors for the preparation of bifunctional $PdZn/ZnO/\gamma\text{-}Al_2O_3$ or $Pd_2Ga/Ga_2O_3/\gamma\text{-}Al_2O_3$ catalysts, respectively, for the STD process.[8] The active Pd_2Ga or PdZn intermetallic phase for CO-to-methanol hydrogenation in these catalysts is formed during reductive catalyst pre-treatment. Pd has also been shown to exhibit synergistic effects in methanol synthesis when combined with various metal oxides such as In_2O_3, Ga_2O_3, ZrO_2, La_2O_3, or CeO_2. CeO_2 is widely used in heterogeneous catalysis as a catalyst or support, due to its unique redox properties and extremely high oxygen storage capacity (OSC).[9] CeO_2-supported Pd catalysts were highly active in CO[10] or CO_2[11] hydrogenation to methanol. CeO_2 was also shown to promote the STD reaction in $Pd/\gamma\text{-}Al_2O_3$ catalysts.[10d] The preparation route played a crucial role, with higher reaction rates

[*] Dr. B. Wang, N. Da Roit, Dr. M. Zimmermann, Prof. Dr. S. Behrens
Institute of Catalysis Research and Technology (IKFT)
Karlsruhe Institute of Technology (KIT)
Hermann-von-Helmholtz-Platz 1, D-76344 Eggenstein-Leopoldshafen
E-mail: silke.behrens@kit.edu
Z. Yu, Dr. S. Chen, Dr. Y. Wang
Institute of Functional Interfaces (IFG)
Karlsruhe Institute of Technology (KIT)
Hermann-von-Helmholtz-Platz 1, D-76344 Eggenstein-Leopoldshafen
E-mail: yuemin.wang@kit.edu
Dr. D. Schild
Institute for Nuclear Waste Disposal (INE)
Karlsruhe Institute of Technology (KIT)
Hermann-von-Helmholtz-Platz 1, D-76344 Eggenstein-Leopoldshafen

observed for Pd/CeO_2 catalysts prepared by decomposition-precipitation compared to conventional impregnation.[12] The combination of Pd/CeO_2 with solid acids in bifunctional catalysts seems to be very promising.[13] However, achieving superior performance in the single-step synthesis of DME using Pd/CeO_2-based catalysts remains a significant challenge, and there is still a lack of profound insight into the nature of the active sites.

Herein, we report the synthesis of novel bifunctional catalysts based on $Pd/CeO_2/\gamma\text{-}Al_2O_3$ with significantly improved reaction rates and DME yields in the STD reaction. The catalysts are prepared using the 'precursor' concept, where colloidal Pd nanoparticles in a CeO_2 matrix are used as building blocks for the methanol-active component and are successively deposited on the $\gamma\text{-}Al_2O_3$ dehydration catalyst. We show that the reaction rates are highly dependent on the preparation route. Catalysts obtained via colloidal routes resulted in a high concentration of Pd/CeO_2 interfacial sites and high reaction rates, while for Pd deposited on commercial ceria the reaction rates were much lower. The catalytic performance was evaluated in a fixed bed reactor at 50 bar using simulated, biomass-derived syngas (inert gases: $CO:H_2=7:1.5:1.5$). The active sites were characterized using temperature-dependent ultrahigh vacuum Fourier-transform infrared spectroscopy (UHV-FTIRS).

Results and Discussion

The bifunctional STD catalysts were prepared using the 'precursor' concept, where colloidal NPs are synthesized in solution in a first step and then deposited as methanol-active component on the $\gamma\text{-}Al_2O_3$ dehydration catalyst (Figure 1). Pd NPs embedded in a nanoparticulate CeO_2 matrix (i.e., Pd/CeO_2 NPs) were synthesized, in addition to the Pd and CeO_2 NPs prepared for the respective reference catalysts (see Supporting Information). The Pd and CeO_2 NPs were obtained by thermolysis of palladium (II) or cerium (III) acetylacetonate, respectively, in oleyl amine (OLAM) in the presence of trioctylphosphine (TOP) ligands, as previously described by us for Pd NPs.[14] The Pd/CeO_2 and Pd/ZrO_2 NPs were synthesized by a similar one-pot procedure via the co-decomposition of the respective palladium (II) and cerium (III) or zirconium (IV) precursors, resulting in the formation of Pd NPs dispersed in a nanoparticulate CeO_2 or ZrO_2 matrix, respectively. Similarly, Cu/CeO_2 NPs were prepared by co-decomposing copper (II) and cerium (III) precursors.

Transmission electron microscopy (TEM) images of the Pd NPs (Figure 2 a) revealed small, uniform and spherical NPs with an average particle size of 5.5 ± 0.7 nm, while the CeO_2 NPs (Figure 2b) had an average size of 13.9 ± 3 nm. For the Pd/CeO_2 NPs (Figure 2c), spherical Pd particles with a mean size of 5.3 ± 0.9 nm were dispersed in the nanoparticulate CeO_2 matrix. Similarly, the Pd/ZrO_2 NPs (Figure S1a, b) showed spherical Pd NPs (3.7 ± 0.7 nm) dispersed in a nanoparticulate ZrO_2 matrix. For Cu/CeO_2 NPs (Figure S2a), Cu NPs could not be distinguished from nanoparticulate CeO_2. The powder X-ray diffraction (XRD) pattern (Figure 2d) of the Pd and CeO_2 NPs revealed broad reflections of low intensity assigned to the face-centered cubic (fcc) Pd phase (ICDD 00-046-1043) and the fcc CeO_2 phase (ICDD 00-034-0394), respectively. As for Pd/CeO_2 NPs, both the reflections of the fcc Pd phase and the fcc CeO_2 phase were detected, with no reflections remaining unassigned. Similarly, the reflections of metallic Pd and ZrO_2 were also detected for Pd/ZrO_2 NPs (Figure S1c). For Cu/CeO_2 NPs (Figure S2b), sharp reflections of metallic Cu (ICDD 01-085-1326) were observed, indicating larger crystallite sizes.

In a next step, the bifunctional STD model catalysts were synthesized by incipient wetness impregnation where the NPs were deposited on the $\gamma\text{-}Al_2O_3$ dehydration catalyst (see SI). The Pd/CeO_2 NPs were used to prepare the bifunctional PdCe(8)-A catalyst, along with the reference catalysts Pd(8)-A and Ce(24)-A) using only Pd or CeO_2 NPs, respectively. In addition, the Pd NPs were supported on commercial CeO_2 and then added to the $\gamma\text{-}Al_2O_3$ dehydration catalyst to generate the PdCe(8)-A_(C) reference catalyst. The PdZr(7)-A and CuCe(6)-A catalysts were prepared from Pd/ZrO_2 and Cu/CeO_2 NPs in a similar manner to PdCe(8)-A. All bifunctional catalysts were calcined at 350 °C to remove any organic residues from the NP synthesis. The Pd loading of the bifunctional catalysts ranged from 5.6 to 8.4 wt.% (Table S2) with a homogeneous distribution of Pd on $\gamma\text{-}Al_2O_3$ (Figure S3). As expected, all

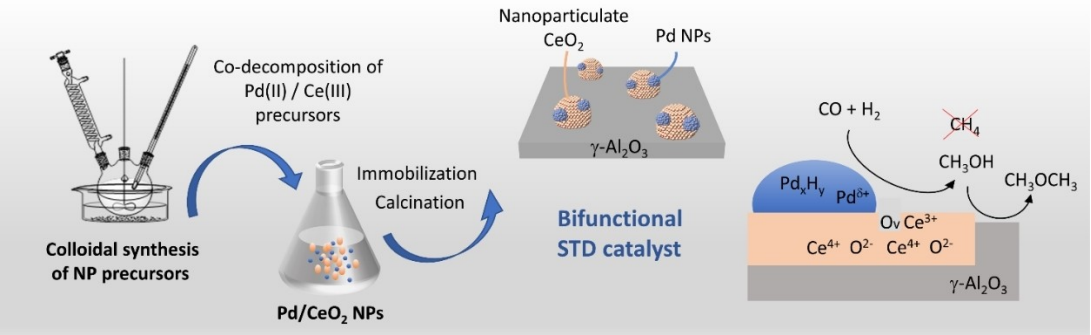

Figure 1. Bifunctional $Pd/CeO_2/Al_2O_3$ catalysts have been prepared using the 'precursor' concept where colloidal NPs are used as building blocks for the methanol-active component. The highly dispersed and spatially confined small Pd NPs, together with their strong electronic interaction with the nanoparticulate CeO_2 matrix, lead to a superior performance in terms of activity, DME selectivity, and stability for the STD reaction.

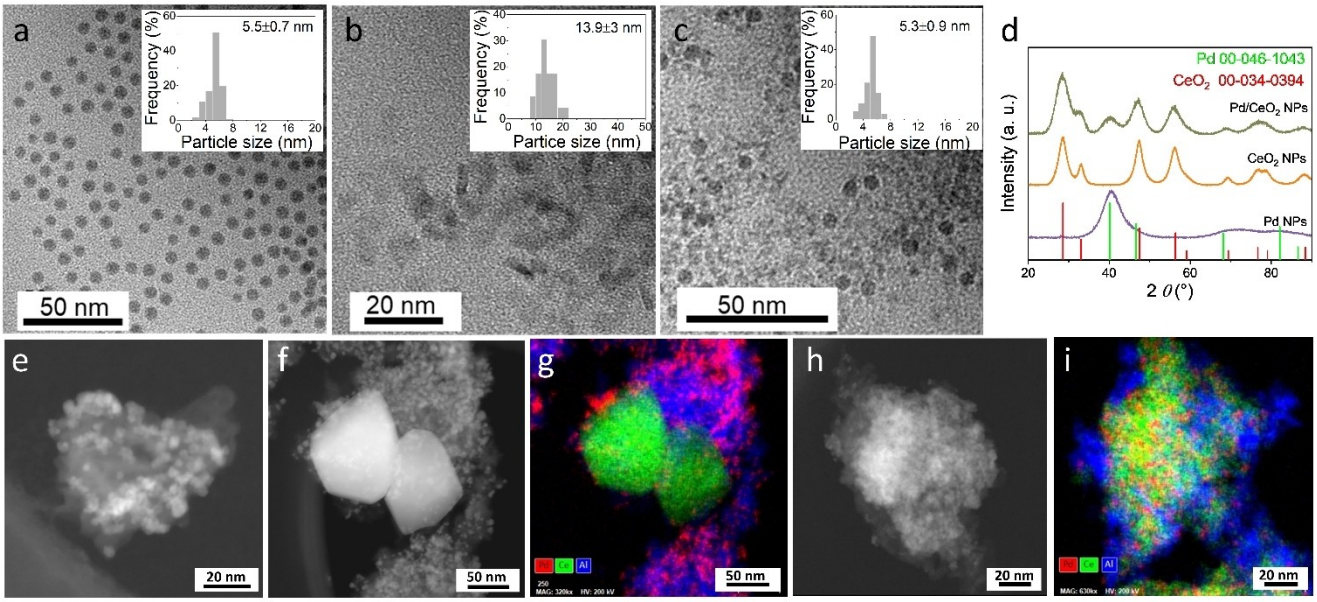

Figure 2. TEM images with size histograms of (a) Pd NPs, (b) CeO_2 NPs, and (c) Pd/CeO_2 NPs. (d) XRD patterns of the nanoparticles isolated as a powder after NP synthesis. HAADF-STEM images with EDS elemental mapping of the calcined (e) Pd(8)-A, (f, g) PdCe(8)-A_(C) and (h, i) PdCe(8)-A catalysts (red: Pd; green: Ce; blue: Al).

catalysts except PdZr(7)-A showed lower surface areas compared to γ-Al_2O_3, with the smallest surface areas for catalysts prepared using Pd NPs and commercial ceria (PdCe(8)-A_(C)).

High-angle annular dark-field scanning TEM (HAADF-STEM) images with elemental mapping show the NPs (PdO after calcination) in close contact with the nanoparticulate CeO_2 matrix, both homogeneously distributed on γ-Al_2O_3 for the calcined PdCe(8)-A catalyst (Figure 2h, i). The HAADF-STEM images confirmed that no large PdO particles were detected for the calcined catalyst, although a few larger Pd particles were observed for the spent catalyst after 40 h of time-on-stream (TOS), which were mainly located on the γ-Al_2O_3 (Figure S4). Importantly, the small Pd NPs were mostly preserved in close contact with the nanoparticulate CeO_2 matrix (Figure S4c). However, for the calcined PdCe(8)-A_(C) (Figure 2f, g) reference catalyst, the PdO NPs appeared to be mainly distributed over the γ-Al_2O_3 dehydration catalyst, similar as Pd(8)-A (Figure 2e), while only a few were detected on the large commercial CeO_2 particles. In contrast to PdCe(8)-A, both the PdCe(8)-A_(C) and Pd(8)-A reference catalysts as well as PdZr(7)-A also showed more pronounced sintering behavior (Figure S4a, b and Figure S5).

The corresponding XRD analysis of the calcined Pd(8)-A, PdCe(8)-A and PdCe(8)-A_(C) catalysts revealed the reflections of PdO (ICDD 00-041-1107) and γ-Al_2O_3 (ICDD 00-010-0425) (Figure S6a). In addition, consistent with the HAADF-STEM observations, the PdCe(8)-A catalyst also showed broad, low-intensity reflections of the fcc CeO_2 phase, characteristic of small ceria crystallites. In pronounced contrast, for the PdCe(8)-A_(C) reference catalyst based on commercial CeO_2, the reflections of the CeO_2 phase were much sharper and of higher intensity due to the larger crystallite sizes (for XRD patterns of PdZr(7)-A and CuCe(6)-A, see Figures S7 and Figure S8). After the catalytic tests (Figure 3a and Figure S6b), the spent Pd(8)-A and PdCe(8)-A_(C) catalysts showed reflections at 40.1° and 39.1° (2 θ) of the fcc Pd and Pd_xH_y phases (ICDD 01-087-0637), in addition to those of CeO_2 and γ-Al_2O_3, confirming the PdO reduction during catalyst activation and testing. The reflections of Pd_xH_y were also detected for spent PdCe(8)-A, while the existence of metallic Pd cannot be completely excluded due to the small size of the Pd nanoparticles and some overlap with γ-Al_2O_3 reflections (see Figure S6c). Note that the reflections may shift depending on the amount of interstitial hydrogen. The reflections of the Pd_xH_y phase but none of the fcc Pd phase, were

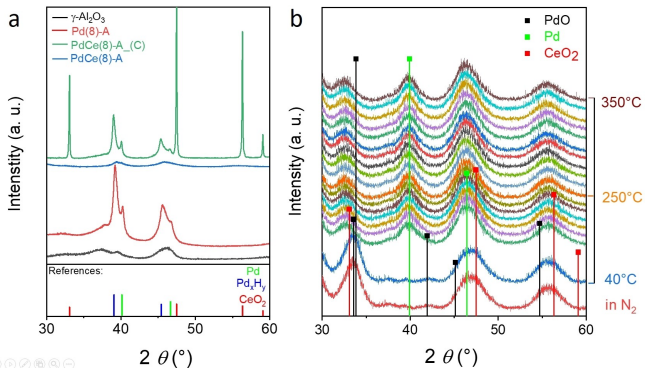

Figure 3. XRD patterns of (a) the spent STD catalysts after the catalytic tests with magnification for Bragg angles of 30 to 60° (2θ). (b) Analysis of the activation process of PdCe(8)-A catalysts in H_2 atmosphere (2 vol.% in N_2) by in situ XRD (XRD patterns were recorded every 30 °C for temperatures of 40–250 °C and every 10 °C for temperatures of 250–350 °C).

observed for the spent PdZr(7)-A catalysts (Figure S7). The Pd_xH_y crystallite sizes, calculated using the Scherrer equation and the (111) reflection (39.1° (2θ)), were smallest at 9 nm for the PdCe(8)-A catalyst and significantly larger for the two spent reference catalysts, 32 nm for PdCe(8)-A_(C) and 16 nm for Pd(8)-A. This finding indicates a spatially confined effect for the PdCe(8)-A catalyst, where the nanoparticulate CeO_2 matrix limited the aggregation of Pd particles during the STD process (Table S2). Although the PdO particles of calcined PdZr(7)-A were also in intimate contact with the ZrO_2 matrix homogeneously distributed on γ-Al_2O_3 (Figure S5), the sintering of Pd_xH_y particles (crystallite size 23 nm) was more severe compared to PdCe(8)-A. It should be noted that an Pd_xH_y phase was not formed and observed by in situ XRD analysis of the PdCe(8)-A and Pd(8)-A catalysts under H_2 atmosphere (2 vol.% H_2 in nitrogen) at atmospheric pressure (Figure 3b and Figure S6d), indicating Pd_xH_y formation under the conditions of the catalyst tests at high H_2 and CO pressures. For the spent CuCe(6)-A catalyst (Figure S8), metallic Cu and fcc CeO_2 phases were detected (for XRD pattern of Ce(24)-A reference see Figure S6).

X-ray photoelectron spectroscopy (XPS) analysis was performed on the Pd(8)-A, PdCe(8)-A_(C) and PdCe(8)-A catalysts, which were activated in an H_2 atmosphere. Figure 4 shows the corresponding fitted Pd 3d and Ce 3d XPS data. The Pd 3d spectra for Pd(8)-A and PdCe(8)-A_(C) are dominated by a spin-orbit doublet ($3d_{5/2}$ and $3d_{3/2}$) at 335.1/340.4 eV, confirming the presence of metallic Pd^0 species (Figure 4a). Notably, for the PdCe(8)-A catalyst, a second $3d_{5/2}$ and $3d_{3/2}$ doublet was clearly resolved at 336.9/342.2 eV, characteristic of the partially oxidized Pd^{2+} species.[15] The Ce 3d spectra of reduced PdCe(8)-A_(C) and PdCe(8)-A were complex and could be classified into two sets of spin-orbit multiplets (Figure 4b): the "*v*" group and the "*u*" group, representing the $3d_{5/2}$ and $3d_{3/2}$ spectra of Ce, respectively. The three 3d doublets, *v*/*u*, *v*″/*u*″, and *v*‴/*u*‴, originate from Ce^{4+}, while the two doublets, v_0/u_0 and *v*′/*u*′, correspond to the 3*d* peaks of Ce^{3+}.[10a,13a,16] For the reduced

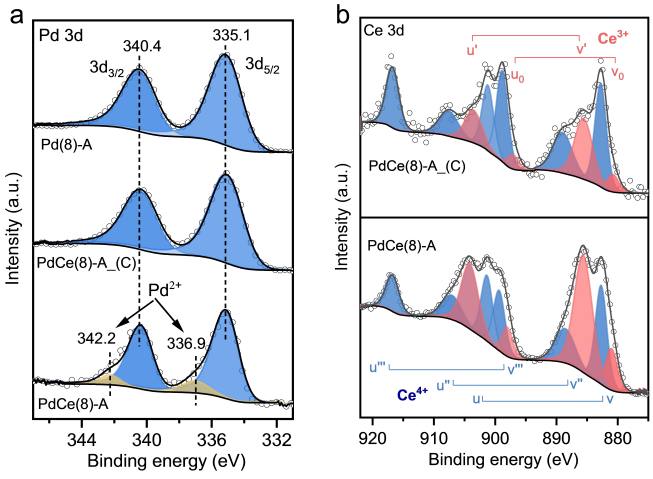

Figure 4. XPS spectra with curve fits of the reduced bifunctional STD catalysts: (a) Pd 3d and (b) Ce 3d.

PdCe(8)-A and PdCe(8)-A_(C) catalysts, the Ce cations in the ceria were present in a mixed valence state of both Ce^{3+} and Ce^{4+}, but the catalysts derived from our Pd/CeO_2 NPs on γ-Al_2O_3 revealed a higher proportion of Ce^{3+} species (49 %) compared to Pd NPs on commercial ceria (29 %). This is most likely due to the intimate contact between Pd and the nanoparticulate CeO_2 matrix. Consequently, the strong electronic interactions between Pd and ceria lead to the formation of partially oxidized Pd^{2+} and reduced Ce^{3+} species. The Pd^{2+} concentration was estimated to be approximately 15 %. For PdZr(7)-A, its Pd 3d and Zr 3d (Figure S9) spectra were in good agreement with metallic Pd and ZrO_2, respectively.

The structural and electronic properties of the Pd-based catalysts were further investigated using in situ UHV-FTIR spectroscopy (low-temperature IR transmission). This highly surface-sensitive and non-destructive approach is well-suited for characterizing the intrinsic properties of metal/oxide nanoparticles.[17] As shown in Figure 5a and b, after CO adsorption at 125 K, both Pd(8)-A and PdCe(8)-A_(C) samples show a dominant IR band at approximately 1995 cm^{-1}, characteristic of bridge CO species bound to two neighboring Pd^0 atoms.[15,17b] In addition, a weak band appears at about 2100 cm^{-1} originating from linearly bonded on-top CO–Pd as minority species.[15] These findings reveal the formation of relatively large, metallic Pd nanoparticles as the predominant species on both Al_2O_3 and commercial ceria powder samples. In pronounced contrast, the UHV-FTIRS data of CO adsorbed on PdCe(8)-A show numerous distinct IR bands with comparable intensities (Figure 5c). In addition to the bridge-bonded CO on contiguous Pd atoms (1989 cm^{-1}, 1945 cm^{-1}), the on-top CO–Pd band at 2102 cm^{-1} becomes significantly intense. These results provide direct evidence for small Pd clusters highly dispersed on the surface of the nanoparticulate ceria matrix. More importantly, positively charged Pd cations were identified by the characteristic CO vibration at 2140 cm^{-1},[15] revealing strong electronic interactions between Pd and ceria matrix. This is further supported by the observation of a high-lying CO band at 2186 cm^{-1}, which is assigned to CO adsorbed at reduced Ce^{3+} sites in the vicinity of Pd^{2+} sites,[17b] similar to observations in Pt/CeO_2 systems.[17d] It should be emphasized that this band is absent in the IR spectra of the Pd(8)-A and PdCe(8)-A_(C) catalysts. The weak signal at 2203 cm^{-1} is ascribed to CO bound to Al^{3+} sites on the Al_2O_3 support.

The presence of various CO species on PdCe(8)-A is further demonstrated by the temperature-resolved UHV-FTIRS data, which provide insights into the thermal stability of distinct CO adsorbates. The corresponding IR results are shown in Figure 5d. Figure 5e presents a quantitative analysis of the relative intensity of various CO bands across different temperatures. CO molecules are weakly bound to surface Al^{3+} and Ce^{3+} cations, primarily via electrostatic interactions and electron donation, and desorb almost entirely at approximately 150 K. The CO–Pd^{2+} band at 2140 cm^{-1} vanishes after heating to 220 K, indicating a higher binding energy compared to CO adsorbed on Al^{3+} and Ce^{3+} species. This is attributed to the additional

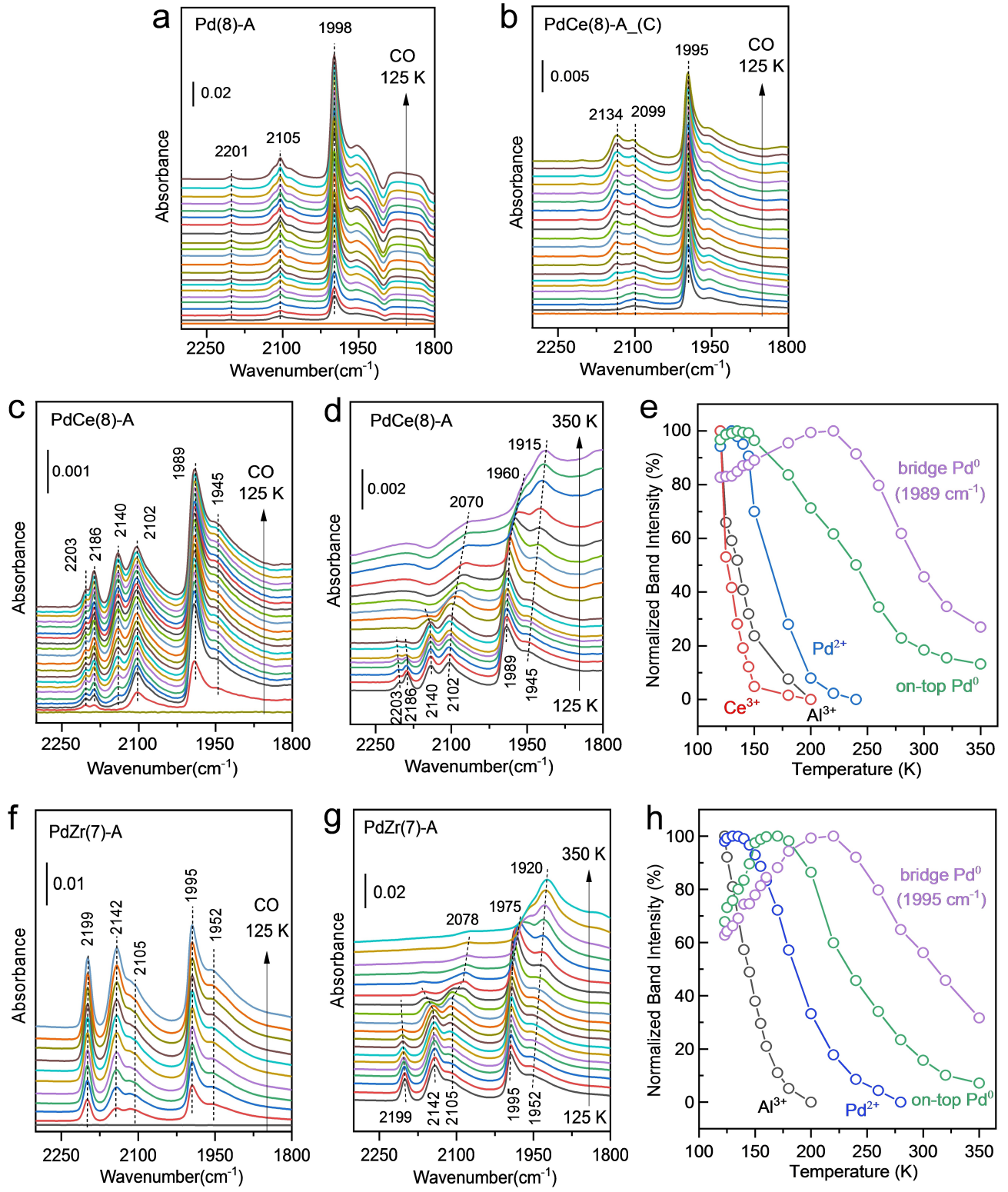

Figure 5. In situ UHV-FTIR spectra of CO (1×10^{-3} mbar) adsorbed at 125 K on various Pd-related catalysts: (a) Pd(8)-A; (b) PdCe(8)-A_(C); (c–e) PdCe(8)-A; (f-h) PdZr(7)-A. Consecutive spectra were recorded at 2-minute intervals. Thermal stability of various CO species adsorbed on (d) PdCe(8)-A and (g) PdZr(7)-A was monitored via temperature-dependent IR spectra. Evolution of CO band intensities on (e) PdCe(8)-A and (h) PdZr(7)-A is presented as a function of sample temperature.

contribution of electron back-donation. CO adsorbs more strongly on metallic Pd sites (both on-top and bridge sites), where the CO–Pd interactions are dominated by electron back-donation. Interestingly, the Pd^0-related CO bands

become more intense as the CO–Pd^{2+} band weakens (Figure 5e), suggesting the thermal diffusion of adsorbed CO molecules from cationic to metallic palladium sites.[15,18] The CO–Pd^0 bands gradually decrease in intensity as the sample temperature rises further and are still visible at 350 K. The attenuation of the on-top and bridge-bonded CO–Pd^0 species is accompanied by a red-shift in frequency. This coverage-induced frequency shift is typical for CO adsorption on metallic Pd sites and can be explained in terms of adsorbate-adsorbate interactions, involving chemical shift and dipole-dipole coupling effects.[19] In contrast, upon heating to higher temperatures (i.e., decreasing coverage), a blue shift was observed for the IR bands of CO adsorbed on Al^{3+}, Ce^{3+}, and Pd^{2+} cations (Figure 5d), originating from dynamic and substrate-mediated static interactions between the adsorbed CO molecules.[20]

For comparison, Figure 5f displays the in situ UHV-FTIRS data collected during CO adsorption on PdZr(7)-A at 125 K. The IR signals correspond to CO bound to surface Al^{3+} (2199 cm^{-1}), on-top Pd^0 (2105 cm^{-1}) and bridge Pd^0 (1995 and 1952 cm^{-1}) sites, with cationic Pd^{2+} detected as the predominant species (2142 cm^{-1}). These assignments are further corroborated by the temperature-induced spectral evolution (see Figure 5g, h), in line with observations for PdCe(8)-A (Figure 5d, e). The presence of Pd^{2+} species indicates strong electronic interactions between Pd and the ZrO_2 support, as discussed above. We note that the IR band of CO adsorbed on reduced $Zr^{\delta+}$ species may overlap with the CO–Pd^0 band around 2100 cm^{-1}. It has been reported that this band appears at ~2085 cm^{-1} on reduced ZrO_2 surfaces.[21]

After activation of the STD catalysts in H_2 atmosphere, the catalytic performance was investigated in the STD reaction over a temperature range of 250 °C to 350 °C at 50 bar using a continuous fixed-bed reactor and CO-rich syngas (inert gases: $CO:H_2=7:1.5:1.5$) (Figure 6, Figure S10, Figure S11, Figure S12 and Table S3). In general, the PdCe(8)-A catalyst revealed a significantly higher catalytic activity than the two reference catalysts Pd(8)-A and PdCe(8)-A_(C), whereas Ce(24)-A showed no activity. At 250 °C, all catalysts showed a high DME selectivity in the range of 61.8 % to 66.1 % (Figure 6b), while the PdCe(8)-A catalyst revealed a lower methanol selectivity comparable to CuCe(6)-A (S_{MeOH}: 1.9 % (PdCe(8)-A), 7.2 % (PdCe(8)-A_(C)), 8.7 % (Pd(8)-A), 5.2 % (PdZr(7)-A), 1.1 % (CuCe(6)-A)). It is known that Pd^0 can promote the methane formation during CO hydrogenation, and methane was formed in all cases. The CH_4 selectivity increased from PdCe(8)-A (4.2 %) over PdZr(7)-A (7.9 %), PdCe(8)-A_(C) (11.3 %) to Pd(8)-A (11.5 %), indicating that the contact to the nanoparticulate CeO_2 matrix effectively limited CH_4 formation. Based on the XPS and IR analysis, this could be related to the presence of highly dispersed Pd clusters/particles with interfacial $Pd^{\delta+}$ species. In comparison, for Pd particles supported on TiO_2, the methane selectivity was up to 25 % at 260 °C in methanol synthesis via CO hydrogenation.[22] In addition, the PdCe(8)-A catalyst (X_{CO}

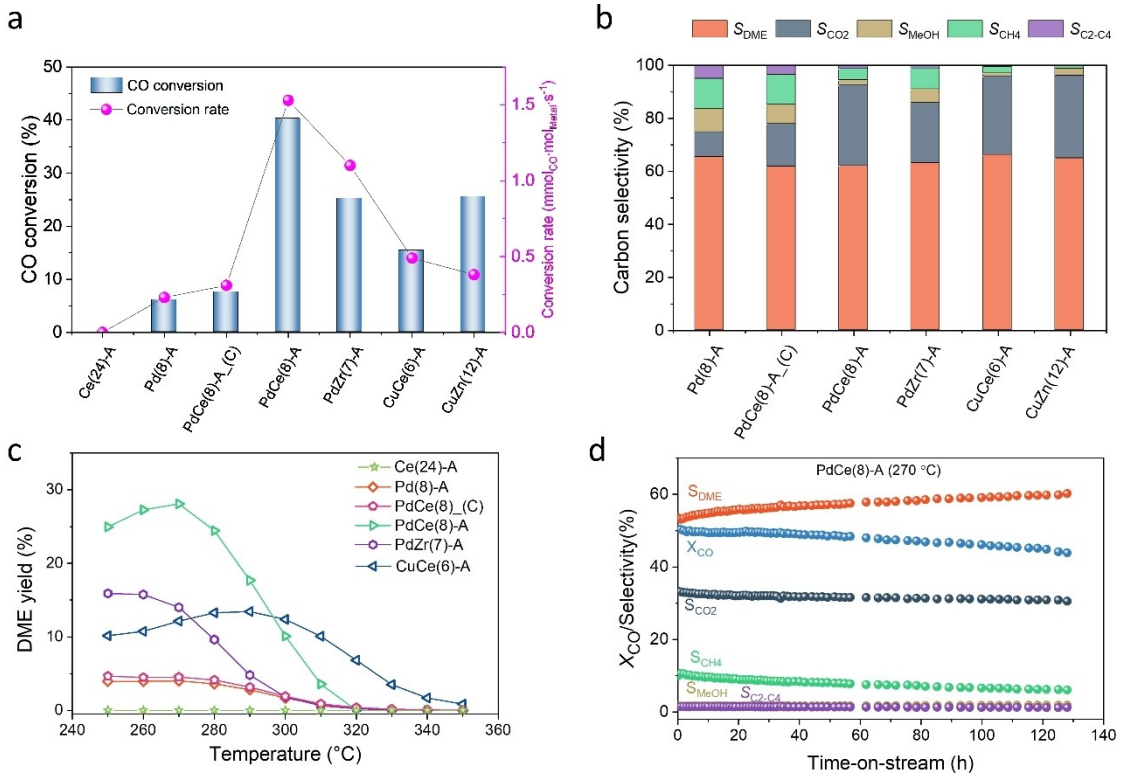

Figure 6. Catalytic performance of the bifunctional Pd(8)-A, PdCe(8)-A_(C), and PdCe(8)-A catalysts as compared to the PdZr(7)-A, CuCe(6)-A, and CuZn(12)-A[20] catalysts: (a) CO conversion / conversion rate and (b) carbon selectivities at 250 °C; (c) DME yields as a function of temperature; (d) CO conversion and carbon selectivities on the PdCe(8)-A catalyst over TOS (reaction temperature 270 °C).

40.3 %) (Figure 6a) revealed a significantly higher CO conversion than the Pd(8)-A (X_{CO} 6.0 %) and PdCe(8)-A_(C) (X_{CO} 7.5 %) reference catalysts. Consequently, the DME yield (Figure 6c) of PdCe(8)-A (Y_{DME} 25.0 %) was much higher than those of PdCe(8)-A_(C) (Y_{DME} 4.7 %) and Pd(8)-A (Y_{DME} 3.9 %). The CO conversion of PdCe(8)-A was also higher than those of the Pd/ZrO_2-based and Cu/CeO_2-based catalysts, prepared using a similar synthesis approach. In particular, when compared to previously reported results of Cu/ZnO-based catalysts,[23] the conversion rate (normalized to the amount of metal (Pd or Cu) in mol) (Figure 6a) of PdCe(8)-A was four times that of the Cu/Zn catalyst. The proper addition of CeO_2 can improve the Pd dispersion and hence increase the CO conversion in the STD reaction.[13b]

With increasing temperature, the DME selectivity and DME yield experienced a decrease due to methane formation (Figure S11c–g), although CO conversion was promoted. Moreover, PdCe(8)-A experienced a slower decrease in DME selectivity compared to the PdCe(8)-A_(C) and Pd(8)-A reference catalysts, again suggesting that the intimate contact between Pd NPs and nanoparticulate CeO_2 limited the CH_4 formation. Based on this increase in CO conversion (X_{CO} 48.1 %), PdCe(8)-A reached the highest DME yield at 270 °C (Y_{DME} 28.1 %), approaching the equilibrium CO conversion (X_{eq} 54.1 %), while the maximum DME yield was 4.0 % (at 270 °C), 4.7 % (at 250 °C) and 15.9 % (at 250 °C) for the Pd(8)-A and PdCe(8)-A_(C) reference catalysts and PdZr(7)-A, respectively. As the temperature continued to increase, the DME yield decreased, with CH_4 becoming the main reaction product ($S_{CH4} > 45$ %, Table S3). Temperature played a critical role in CH_4 formation and no CH_4 (S_{CH4} 0 %) was formed on the PdCe(8)-A catalyst at 220 °C (Figure S11h). In addition to the reaction temperature, a decrease in residence time ($\tau = m_{catalyst} \cdot V_{total\ gas\ flow}^{-1}$) increased the DME selectivity (Figure S13). By decreasing τ from 2.4 $g \cdot s \cdot mL^{-1}$ to 0.8 $g \cdot s \cdot mL^{-1}$, the DME selectivity of PdCe(8)-A increased from 52.6 % to 62.1 % (280 °C), while the methane selectivity decreased from 11.0 % to 4.1 %.

The stability of the PdCe(8)-A catalyst over TOS was investigated at 270 °C, where the DME yield was maximum in the previous experiments. Only a slight decrease in CO conversion from initially 50.6 % to 44.0 % was observed after 130 h TOS (Figure 6d), revealing the high catalyst stability. The HAADF-STEM images (Figure 2h, Figure S4c in the SI) showed few sintered Pd NPs after catalytic tests, which may cause catalyst deactivation along with coke deposition on active sites due to degradation of reaction intermediates.[24] The CO_2, MeOH and C_2–C_4 selectivities remained stable, while the CH_4 selectivity slightly decreased from 9.9 % to 6.0 % and the DME selectivity gradually increased from 53.6 % to 60.0 % over TOS, reaching a steady state after 80 h TOS. Such an induction period has been previously reported for methanol synthesis from syngas over Pd/CeO_2 catalysts.[10b,13a]

For PdCe(8)-A, the Pd particles were well dispersed in the CeO_2 matrix as visualized by HAADF-STEM (Figure 2h, i). Furthermore, the XPS and UHV-FTIRS data (Figure 4 and Figure 5) consistently revealed the strong electronic interactions between Pd and ceria matrix in the PdCe(8)-A catalyst, yielding positively charged Pd^{2+} and reduced Ce^{3+} species. Importantly, the reduction of Ce cations was accompanied by the creation of O vacancies. Cationic Pd species have been suggested to be the active species for the methanol synthesis from CO.[25] Moreover, the interfacial contact area between Pd and ceria provides CO adsorption sites, which is crucial for CO conversion.[10c,26] Overall, our comprehensive experimental results suggest that the highly dispersed $Pd^{\delta+}$ species, along with the O vacancies at the Pd-ceria interface, account for the high CO conversion and stability in the STD reaction observed with the PdCe(8)-A catalyst.

Conclusions

Pd/CeO_2 particles were synthesized in which small and uniform Pd nanoparticles with mean size of 5.3 nm were dispersed in a matrix of nanoparticulate CeO_2. They were used as the building units for the methanol-active component and immobilized on γ-Al_2O_3 as the dehydration catalyst to obtain bifunctional model catalysts for the direct single-step synthesis of DME from syngas. The bifunctional $Pd/CeO_2/\gamma$-Al_2O_3 catalyst showed a superior catalytic activity and stability in the STD reaction, reaching a DME yield of 28.1 % at 270 °C, more than six times higher than the respective reference catalysts where Pd nanoparticles were supported either directly on γ-Al_2O_3 or on commercial CeO_2 and combined with γ-Al_2O_3. In particular, at low reaction temperatures (250 °C), the DME yield was significantly higher for the $Pd/CeO_2/\gamma$-Al_2O_3 compared to the respective $Cu/ZnO/\gamma$-Al_2O_3 and $Cu/CeO_2/\gamma$-Al_2O_3 catalysts. When normalized by the active metal content (in mol), its reaction rate is more than four times that of the conventional Cu/Zn-based STD reference catalyst prepared using Cu/Zn-NPs synthesized by reductive stabilization.[23] The superior performance of the bifunctional $Pd/CeO_2/\gamma$-Al_2O_3 catalyst in activity, DME selectivity, and stability for the STD reaction was attributed to the presence of highly dispersed and spatially confined small Pd clusters/particles, along with their strong electronic interaction with the nanoparticulate CeO_2 matrix. In general, grafting highly defective CeO_x islands onto high surface area supports is a promising strategy not only for stabilizing and trapping active noble metal species, but also for generating highly active bifunctional catalysts. We foresee that the co-decomposition of metal precursors to form metal particles isolated within a nanoparticulate matrix is an effective approach for producing such bifunctional catalysts for other important reactions.

Acknowledgements

This work was supported by the Deutsche Forschungsgemeinschaft (DFG, German Research Foundation)—Project-ID 426888090—SFB 1441 (projects A4, B2 and C2). We thank Armin Lautenbach, Dr. Heike Störmer, Dr. Martin

Peterlechner, Doreen Neumann-Walter, Nikolaj Slaby, Dr. Thomas Otto, and Christian Schmitt for experimental support. B. W. acknowledges his scholarship from the Chinese Scholarship Council (CSC). S. C. is grateful for a Postdoc fellowship donated by the Helmholtz Association and China Postdoctoral Council (OCPC). Open Access funding enabled and organized by Projekt DEAL.

Conflict of Interest

The authors declare no conflict of interest.

Data Availability Statement

TEM, SEM-EDS, XPS, FTIR, XRD, N_2 physisorption and catalytic data included in this manuscript, or online along with metadata, are available at KITopen / RADAR (DOI: 10.35097/4jh897ny0tvjsa2e).

Keywords: palladium · ceria · direct dimethyl ether synthesis · nanoparticles · IR spectroscopy

[1] a) J. T. Sun, I. S. Metcalfe, M. Sahibzada, *Ind. Eng. Chem. Res.* **1999**, *38*, 3868–3872; b) A. M. Namasivayam, T. Korakianitis, R. J. Crookes, K. D. H. Bob-Manuel, J. Olsen, *Appl. Energy* **2010**, *87*, 769–778; c) K. Saravanan, H. Ham, N. Tsubaki, J. W. Bae, *Appl. Catal. B* **2017**, *217*, 494–522.

[2] M.-H. Huang, H.-M. Lee, K.-C. Liang, C.-C. Tzeng, W.-H. Chen, *Int. J. Hydrogen Energy* **2015**, *40*, 13583–13593.

[3] G. R. Moradi, M. Nazari, F. Yaripour, *Fuel Process. Technol.* **2008**, *89*, 1287–1296.

[4] a) Q. Ge, Y. Huang, F. Qiu, S. Li, *Appl. Catal. A* **1998**, *167*, 23–30; b) R. Ahmad, D. Schrempp, S. Behrens, J. Sauer, M. Döring, U. Arnold, *Fuel Process. Technol.* **2014**, *121*, 38–46.

[5] a) X.-J. Tang, J.-H. Fei, Z.-Y. Hou, X.-M. Zheng, H. Lou, *Energy Fuels* **2008**, *22*, 2877–2884; b) J. Ereña, R. Garoña, J. M. Arandes, A. T. Aguayo, J. Bilbao, *Catal. Today* **2005**, *107* (108), 467–473.

[6] G. R. Moradi, S. Nosrati, F. Yaripor, *Catal. Commun.* **2007**, *8*, 598–606.

[7] A. Beck, M. A. Newton, L. G. A. van de Water, J. A. van Bokhoven, *Chem. Rev.* **2024**, *124*, 4543–4678.

[8] a) M. Gentzen, D. E. Doronkin, T. L. Sheppard, A. Zimina, H. Li, J. Jelic, F. Studt, J. D. Grunwaldt, J. Sauer, S. Behrens, *Angew. Chem.* **2019**, *131*, 15802–15806; *Angew. Chem. Int. Ed.* **2019**, *58*, 15655–15659; b) M. Gentzen, D. E. Doronkin, T. L. Sheppard, J. D. Grunwaldt, J. Sauer, S. Behrens, *Appl. Catal. A* **2018**, *562*, 206–214.

[9] a) A. Trovarelli, J. Llorca, *ACS Catal.* **2017**, *7*, 4716–4735; b) T. Montini, M. Melchionna, M. Monai, P. Fornasiero, *Chem. Rev.* **2016**, *116*, 5987–6041; c) M. V. Ganduglia-Pirovano, A. Hofmann, J. Sauer, *Surf. Sci. Rep.* **2007**, *62*, 219–270; d) A. F. Trovarelli, Paolo, *Catalysis by Ceria and Related Materials*, Imperial College Press, **2013**; e) C. Yang, H. Idriss, Y. Wang, C. Wöll, *Acc. Chem. Res.* **2024**, *57*, 3316–3326.

[10] a) Y. Matsumura, W. J. Shen, Y. Ichihashi, M. Okumura, *J. Catal.* **2001**, *197*, 267–272; b) S. Naito, T. Kasahara, T. Miyao, *Catal. Today* **2002**, *74*, 201–206; c) W.-J. Shen, M. Okumura, Y. Matsumura, M. Haruta, *Appl. Catal. A* **2001**, *213*, 225–232; d) X. L. Meng, Y. F. Liu, Z. C. Zhang, R. Z. Chu, Z. M. Zong, X. Y. Wei, *Appl. Mech. Mater.* **2011**, *66* (68), 1193–1198.

[11] a) R. Khobragade, M. Roškarič, G. Žerjav, M. Košiček, J. Zavašnik, N. Van de Velde, I. Jerman, N. N. Tušar, A. Pintar, *Appl. Catal. A* **2021**, *627*, 118394; b) T. Fujitani, I. Nakamura, *Bull. Chem. Soc. Jpn.* **2002**, *75*, 1393–1398.

[12] W. J. Shen, Y. Ichihashi, M. Okumura, Y. Matsumura, *Catal. Lett.* **2000**, *64*, 23–25.

[13] a) Y. Ma, Q. Ge, W. Li, H. Xu, *Appl. Catal. B* **2009**, *90*, 99–104; b) S. Imamura, H. Yamane, H. Kanai, Y. Saito, K. Utani, *J. Jpn. Petrol. Inst.* **2002**, *45*, 222–229.

[14] a) V. R. Naina, S. Wang, D. I. Sharapa, M. Zimmermann, M. Hähsler, L. Niebl-Eibenstein, J. Wang, C. Wöll, Y. Wang, S. K. Singh, F. Studt, S. Behrens, *ACS Catal.* **2021**, *11*, 2288–2301; b) S. Wang, D. E. Doronkin, M. Hähsler, X. Huang, D. Wang, J.-D. Grunwaldt, S. Behrens, *ChemSusChem* **2020**, *13*, 1–10.

[15] G. Tofighi, X. Yu, H. Lichtenberg, D. E. Doronkin, W. Wang, C. Wöll, Y. Wang, J.-D. Grunwaldt, *ACS Catal.* **2019**, *9*, 5462–5473.

[16] a) M. Romeo, K. Bak, J. El Fallah, F. Le Normand, L. Hilaire, *Surf. Interface Anal.* **1993**, *20*, 508–512; b) E. Paparazzo, *J. Phys. Condens. Matter* **2018**, *30*, 343003.

[17] a) Y. Wang, C. Wöll, *Chem. Soc. Rev.* **2017**, *46*, 1875–1932; b) D. Gashnikova, F. Maurer, E. Sauter, S. Bernart, J. Jelic, P. Dolcet, C. B. Maliakkal, Y. Wang, C. Wöll, F. Studt, C. Kubel, M. Casapu, J. D. Grunwaldt, *Angew. Chem. Int. Ed.* **2024**, *63*, e202408511; c) C. Yang, M. Capdevila-Cortada, C. Dong, Y. Zhou, J. Wang, X. Yu, A. Nefedov, S. Heissler, N. Lopez, W. Shen, C. Wöll, Y. Wang, *J. Phys. Chem. Lett.* **2020**, *11*, 7925–7931; d) F. Maurer, J. Jelic, J. Wang, A. Gänzler, P. Dolcet, C. Wöll, Y. Wang, F. Studt, M. Casapu, J.-D. Grunwaldt, *Nat. Catal.* **2020**, *3*, 824–833; e) S. Liu, Y. Li, X. Yu, S. Han, Y. Zhou, Y. Yang, H. Zhang, Z. Jiang, C. Zhu, W. X. Li, C. Wöll, Y. Wang, W. Shen, *Nat. Commun.* **2022**, *13*, 4559.

[18] C. Yang, X. Yu, S. Heißler, A. Nefedov, S. Colussi, J. Llorca, A. Trovarelli, Y. Wang, C. Wöll, *Angew. Chem.* **2017**, *129*, 382–387; *Angew. Chem. Int. Ed.* **2017**, *56*, 375–379.

[19] a) A. Crossley, D. A. King, *Surf. Sci.* **1977**, *68*, 528–538; b) B. N. J. Persson, R. Ryberg, *Phys. Rev. B* **1981**, *24*, 6954.

[20] M. Buchholz, X. Yu, C. Yang, S. Heißler, A. Nefedov, Y. Wang, C. Wöll, *Surf. Sci.* **2016**, *652*, 247–252.

[21] S. Chen, P. N. Plessow, Z. Yu, E. Sauter, L. Caulfield, A. Nefedov, F. Studt, Y. Wang, C. Wöll, *Angew. Chem.* **2024**,*136*, e202404775; *Angew. Chem. Int. Ed.* **2024**, *63*, e202404775.

[22] W.-Y. Kim, H. Hayashi, M. Kishida, H. Nagata, K. Wakabayashi, *Appl. Catal. A* **1998**, *169*, 157–164.

[23] M. Gentzen, W. Habicht, D. E. Doronkin, J. D. Grunwaldt, J. Sauer, S. Behrens, *Catal. Sci. Technol.* **2016**, *6*, 1054–1063.

[24] a) A. T. Aguayo, J. Ereña, I. Sierra, M. Olazar, J. Bilbao, *Catal. Today* **2005**, *106*, 265–270; b) Z. Azizi, M. Rezaeimanesh, T. Tohidian, M. R. Rahimpour, *Chem. Eng. Process. Process Intensif.* **2014**, *82*, 150–172.

[25] a) J. Driessen, *J. Catal.* **1983**, *82*, 26–34; b) R. Burch, P. Hollins, *Catal. Today* **1992**, *12*, 107–111; c) V. Ponec, *Surf. Sci.* **1992**, *272*, 111–117.

[26] a) W. J. Shen, Y. Ichihashi, H. Ando, Y. Matsumura, M. Okumura, M. Haruta, *Appl. Catal. A* **2001**, *217*, 231–239; b) W. J. Shen, A. Kobayashi, Y. Ichihashi, Y. Matsumura, M. Haruta, *Catal. Lett.* **2001**, *73*, 161–165.

Manuscript received: November 28, 2024
Accepted manuscript online: February 25, 2025
Version of record online: March 15, 2025